JACS
JOURNAL OF THE AMERICAN CHEMICAL SOCIETY
pubs.acs.org/JACS Article

Luminescence and Covalency in Ytterbium-Doped CrX_3 (X = Cl, Br, I) van der Waals Compounds

Thom J. Snoeren, Kimo Pressler, Kyle T. Kluherz, Kelly M. Walsh, James J. De Yoreo, and Daniel R. Gamelin*

Cite This: *J. Am. Chem. Soc.* 2023, 145, 17427−17434 Read Online

ACCESS | Metrics & More | Article Recommendations | Supporting Information

ABSTRACT: The layered 2D van der Waals ferromagnets CrX_3 (X = Cl, Br, I) show broad d−d photoluminescence (PL). Here we report preparation, structural characterization, and spectroscopic studies of all three CrX_3 compounds doped with the optical impurity, Yb^{3+}. EXAFS measurements show very similar Cr K-edge and Yb L-edge data for each doped compound, and good fits of the latter are obtained for structures having Yb^{3+} occupying substitutional octahedral sites. Yb−X bond lengths are systematically ~0.25 Å larger than their Cr−X counterparts. 4 K PL measurements show efficient sensitization of Yb^{3+} luminescence upon photoexcitation into lattice absorption bands [Cr^{3+} d−d and ligand-to-metal charge-transfer (LMCT)] for all three compounds, converting their nondescript broadband d−d PL into sharp f−f emission. The PL of $CrCl_3$:Yb^{3+} and $CrBr_3$:Yb^{3+} occurs at energies typical for $[YbX_6]^{3-}$ with these halides, with PL decay times of 0.5−1.0 ms at 4 K, but CrI_3:Yb^{3+} displays anomalously low-energy Yb^{3+} emission and an unusually short PL decay time of only 8 μs at 4 K. Data analysis and angular overlap model (AOM) calculations show that Yb^{3+} in CrI_3:Yb^{3+} has a lower spin−orbit splitting energy than reported for any other Yb^{3+} in any other compound. We attribute these observations to exceptionally high covalency of the Yb^{3+} f orbitals in CrI_3:Yb^{3+} stemming primarily from the shallow valence-shell ionization potentials of the iodide anions.

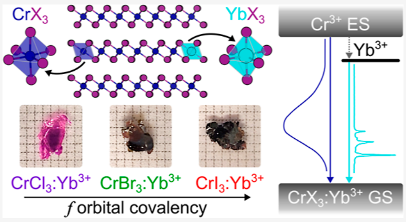

■ INTRODUCTION

The recent demonstration of single-layer ferromagnetism in CrI_3[1] has sparked renewed interest in the CrX_3 (X = Cl, Br, I) family of layered 2D van der Waals materials.[2−4] Although the absorption spectrum of CrI_3 was reported as early as 1965,[5] its photoluminescence (PL) went largely unexplored for decades, and apparently no PL spectra were reported until that of monolayer CrI_3 in 2018.[6] This spectrum shows just a broad nondescript band at the low edge of the visible range, characteristic of Cr^{3+} d−d luminescence in a weak ligand field.[7] Reports on the optical properties of $CrCl_3$ and $CrBr_3$ have followed a similar trajectory, with a handful of absorption[8−10] and reflectivity[11,12] studies dating from the 1960s to 1980s, until the recent pursuit of exfoliable magnetic materials led to a resurgence of interest in their properties.[13,14] The historical lack of attention given to CrX_3 PL likely results from their poor or non-existent emission at room temperature.

Optical doping of CrX_3 compounds has also received little or no attention. Recently, our group communicated the first such results,[15] showing that successful doping of Yb^{3+} ions into bulk CrI_3 yields sharp sensitized Yb^{3+} f−f emission in the near IR. Magneto-PL measurements demonstrated that the Yb^{3+} impurities are strongly magnetically coupled to the CrI_3 host lattice but do not interfere with its ferromagnetic ordering. As a consequence, Yb^{3+} magnetic saturation occurs at external magnetic fields roughly 100× smaller than necessary for Yb^{3+} in diamagnetic lattices. Such intimate magnetic integration of a lanthanide with a ferromagnet implies strong electronic coupling, but remarkably, the electronic structures of Yb^{3+}-doped iodide crystals have received essentially no prior attention, warranting a broader systematic investigation.

Here, we expand upon these initial results by demonstrating successful Yb^{3+} doping of the two magnetic congeners, $CrCl_3$ and $CrBr_3$, establishing the first complete series of lanthanide-doped CrX_3 (X = Cl, Br, I) van der Waals compounds. We show that $CrCl_3$:Yb^{3+} and $CrBr_3$:Yb^{3+} share many of the basic properties of CrI_3:Yb^{3+} but both display higher energy f−f PL with narrower PL line widths and longer PL decay times. Systematic trends across this series of compounds are analyzed in terms of increasing Yb^{3+}−X^- covalency linked to the decreasing anion electronegativities and concomitantly decreasing energies of $X^- \rightarrow Yb^{3+}$ ligand-to-metal charge-transfer (LMCT) excited states in the heavier halides. In addition to illustrating the use of lanthanide dopants to alter the photonic properties of CrX_3 van der Waals ferromagnets, these results highlight the uniquely strong effects of f-orbital covalency in CrI_3:Yb^{3+} relative to other known Yb^{3+} compounds.

Received: June 7, 2023
Published: July 31, 2023

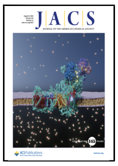

ACS Publications

https://doi.org/10.1021/jacs.3c05989
J. Am. Chem. Soc. 2023, 145, 17427−17434

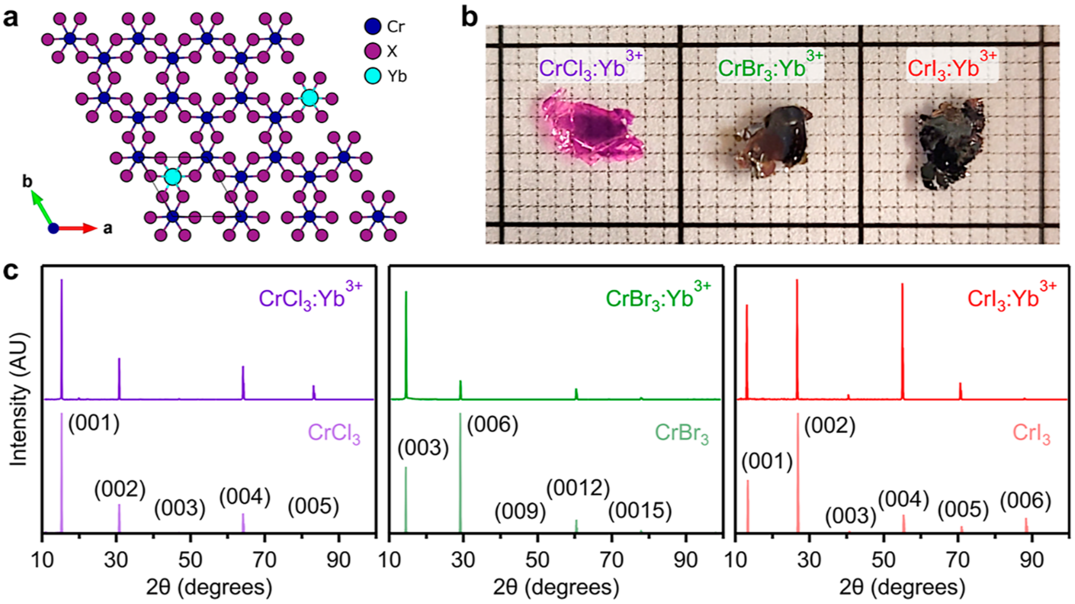

Figure 1. (a) Top-down view of a layer of CrX_3 (X = Cl, Br, I), with Yb^{3+} dopant ions (cyan) substitutionally replacing Cr^{3+} ions (blue) at random sites in the lattice, based on the X-ray crystal structure of CrI_3Yb^{3+}.[15] (b) Photograph of representative as-grown single-crystal flakes of CrX_3 doped with Yb^{3+} on graph paper (minor grid size 1 × 1 mm^2). (c) Room-temperature X-ray diffraction patterns of oriented $CrCl_3$, $CrBr_3$, and CrI_3 single crystals together with their Yb^{3+}-doped counterparts, collected on a powder diffractometer. Due to sample orientation, only $(00l)$ peaks are observed. For monoclinic ($C12/m1$) $CrCl_3$ and CrI_3, $l = n$, for rhombohedral ($R\bar{3}h$) $CrBr_3$ $l = 3n$. At low temperatures, all three materials adopt the $R\bar{3}h$ structure. Cation-relative Yb^{3+} doping concentrations are 2.0, 0.4, and 4.9%, respectively.

RESULTS AND DISCUSSION

Figure 1a depicts a top-down view of a CrX_3 monolayer, showing its honeycomb network lattice structure. In this study, we aimed to replace Cr^{3+} ions with Yb^{3+} impurity ions (cyan) randomly throughout the lattice. To this end, CrX_3 and Yb^{3+}-doped CrX_3 crystals were grown (see Methods) by chemical vapor transport using elemental Cr(0), I_2, and Yb(0) as precursors for CrI_3-based compositions,[15] and using $CrCl_3$, $CrBr_3$, and Yb(0) as precursors for the other halide compositions. Heating these precursors in sealed quartz tubes under a temperature gradient for several days yielded large single-crystal flakes as products. Individual flakes were selected from such samples and used for all of the experiments described here. Figure 1b shows a photograph of representative as-grown flakes of Yb^{3+}-doped CrX_3 (X = Cl, Br, I). Figure 1c shows room-temperature X-ray diffraction patterns of individual oriented CrX_3 flakes and their Yb^{3+}-doped counterparts taken on a powder diffractometer. Only $(00l)$ reflections are observed, consistent with the flakes being single crystals with their out-of-plane axes aligned with the crystallographic *c*-axis. At room temperature, CrI_3 and $CrCl_3$ adopt a monoclinic $C12/m1$ structure, while $CrBr_3$ has an $R\bar{3}h$ space group, which differs from $C12/m1$ only in the offset between layers. At cryogenic temperatures, all three materials exist in the $R\bar{3}h$ phase.[16−18] The Yb^{3+}-doped materials all show small but nonzero shifts in 2θ, consistent with expansion of the unit cells along the soft *c*-axis relative to the undoped parent compound. Yb^{3+} doping concentrations for all measurements detailed in this work are 2.0, 0.4, and 4.9% for X = Cl, Br, and I, respectively, as determined by ICP−MS. EDX data on $CrBr_3:Yb^{3+}$ indicate even distribution of Yb throughout the material (Figure S3).

The ionic radius of Yb^{3+} with six-fold coordination is about 41% larger than that of Cr^{3+},[19] making the possibility of substitutional Yb^{3+} doping uncertain. The local structures of the Cr^{3+} and Yb^{3+} ions were therefore investigated using Extended X-ray Absorption Fine Structure (EXAFS) measurements. Figure 2 shows Fourier-transformed (real-space) EXAFS spectra collected at the Cr K- and Yb L_3-edges of $CrX_3:Yb^{3+}$, for X = Cl, Br, I. Both edges were measured for each sample at room temperature and the data were phase-corrected with their respective single-scattering paths using the Artemis package.[20] The *k*-space EXAFS data (Figure S1) show comparable signal-to-noise ratios for all of the samples described here, as well as a distinct increase in low-*k* features

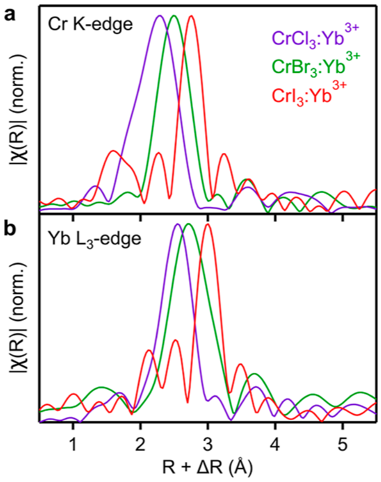

Figure 2. (a) Cr K-edge and (b) Yb L_3-edge Fourier-transformed (real-space) EXAFS data for $CrX_3:Yb^{3+}$ (X = Cl, Br, I) samples. Data are phase-corrected using the respective primary halide scattering paths from fits. Cr peaks are at 2.30, 2.49, and 2.76 Å for Cl, Br, and I data, respectively. Yb peaks are at 2.55, 2.70, and 3.01 Å for Cl, Br, and I data, respectively. Smaller features in the data are consistent with their respective calculated single-scattering paths.

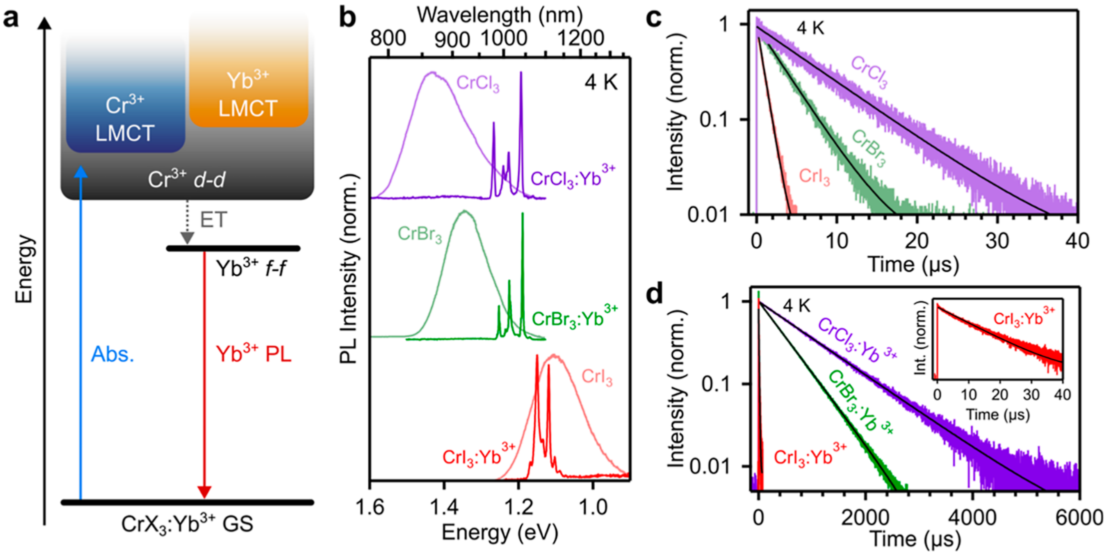

Figure 3. (a) State diagram illustrating absorption and subsequent energy transfer (ET) from excited-state Cr^{3+} to Yb^{3+}, resulting in Yb^{3+} PL. (b) Low-temperature PL spectra of CrX_3 (X = Cl, Br, I) (semi-transparent curves) showing broad $^4T_{2g} \rightarrow {}^4A_{2g}$ luminescence and of their Yb^{3+}-doped counterparts (dark curves) showing sharp $^2F_{5/2} \rightarrow {}^2F_{7/2}$ luminescence. The absence of lattice PL in the latter indicates efficient energy transfer from Cr^{3+} to Yb^{3+}. (c) 4 K time-resolved PL (TRPL) data for CrX_3 compounds. Decay times found from single-exponential fits (black) are 7.42(2), 3.38(4), and 0.84(1) μs for X = Cl, Br, and I, respectively. (d) 4 K TRPL data for CrX_3:Yb^{3+} compounds. Decay times found from single exponential fits (black) are 971.5(6), 501.2(1), and 8.63(1) μs for X = Cl, Br, I, respectively. Inset: enlarged view of the CrI_3:Yb^{3+} decay curve. Yb^{3+} doping concentrations are 2.0, 0.4, and 4.9% for X = Cl, Br, and I, respectively.

moving from Cl to Br to I. These features are consistent with the calculated scattering paths. For all spectra, the features are fit well (Figure S2) by a single-scattering path of the nearest-neighbor halide and indicate octahedral coordination of the metal. Fitting parameters are summarized in Table S1. For both edges, the CrI_3:Yb^{3+} data show additional minority features consistent with an iodide single-scattering path. Overall, these EXAFS data strongly support the presence of $[YbX_6]^{3-}$ octahedra, likely in the form of Yb^{3+} substitution at Cr^{3+} sites. Another possibility is the vacant octahedral interstitial site within the layer,[21] which is differentiated from substitutional sites by having six Cr^{3+} nearest neighbors and threefold coordination of the bridging halides. Yb^{3+} in interstitial sites would require charge compensation, but little interstitial electron density is observed in the single-crystal X-ray structure of CrI_3:Yb^{3+}.[15] These two sites are expected to have similar geometries and hence similar EXAFS signatures.

Looking closer at these results, each spectrum in the Cr K-edge data (Figure 2a) shows a pronounced peak in the range of $R + \Delta R$ = 2−3 Å that can be associated with the Cr−X interatomic spacing. Analysis yields Cr−Cl, Cr−Br, and Cr−I bond lengths of 2.30, 2.49, and 2.76 Å, respectively. These values agree well with crystallographic data, which provide bond lengths of 2.34, 2.52, and 2.72 Å for the same series.[16,18,22] For each sample, the peak in the Yb L_3-edge data (Figure 2b) exhibits a very similar shape to the peak in the corresponding Cr K-edge data but is shifted to higher R values, indicating that all Yb−X bond lengths are elongated by *ca.* 0.25 Å relative to the corresponding Cr−X bond lengths (Yb−Cl, Yb−Br, and Yb−I bond lengths of 2.55, 2.70, and 3.01 Å, respectively). The Yb−X bond lengths found here agree well with those reported for other Yb^{3+} compounds of the same halides.[23−26]

Having clarified their structures, we now turn to the luminescence of these compounds. Figure 3a summarizes overview aspects of the relevant anticipated electronic states of Yb^{3+}-doped CrX_3, including the manifold of Cr^{3+} d−d excited states, the narrow set of Yb^{3+} f−f excited states just below the first Cr^{3+} d−d excited state, and the approximate positions of anticipated Cr^{3+} and Yb^{3+} ligand-to-metal charge-transfer (LMCT) excited states. Figure 3b shows normalized 4 K PL spectra of undoped and Yb^{3+}-doped CrX_3 (X = Cl, Br, I) single-crystal flakes. The undoped materials all show similarly broad Cr^{3+} d−d PL, with peak maxima at 1.43, 1.35, and 1.10 eV, that are consistent with the ligand-field luminescence of other weak-field Cr^{3+} ions. For example, $[CrCl_6]^{3-}$ in Cr^{3+}-doped Cs_2NaYCl_6 shows vibronically broadened PL centered at ~1.38 eV.[7] Figure 3b shows that the broad Cr^{3+} d−d PL is effectively quenched in each of the Yb^{3+}-doped CrX_3 compounds and is replaced by narrow Yb^{3+} f−f emission. The Yb^{3+} PL sensitization scheme is summarized by the arrows in Figure 3a: photoexcitation into the Cr^{3+}-based d−d or LMCT bands is followed by energy transfer to Yb^{3+}, from which f−f emission is observed. Particularly remarkable is the spectrum of 0.4% Yb^{3+}-doped $CrBr_3$, which shows little or no Cr^{3+} luminescence in its CW spectrum despite its relatively low Yb^{3+} concentration. The mean in-plane separation between Yb^{3+} ions in this material is roughly 11 cation sites, indicating that energy migration over these length scales within the Cr^{3+} lattice must be rapid even at 4 K, precluding substantial impedance from traps. CrX_3 compounds can host several native defects[21,27] and energy trapping is likely to affect their native PL in some way, although it is unclear whether any of the observed CrX_3 PL is actually associated with traps. Were this PL from traps, we estimate an upper limit of ~100 meV trapping depth in CrI_3 from comparison of PL and absorption spectra, and even smaller upper limits in $CrBr_3$ and $CrCl_3$, consistent with retention of $[CrX_6]^{3-}$ coordination in each case. As such, trapping is not expected to alter the present analysis or conclusions in any significant way, but may have interesting consequences in energy-migration dynamics. Current work is investigating the energy-migration dynamics that precede energy capture by Yb^{3+} dopants, and these findings will be described in a subsequent report; the present study focuses on characterizing the electronic structures of the Yb^{3+} ions themselves.

Figure 3c shows time-resolved PL (TRPL) data collected for the series of undoped CrX_3 samples measured at 4 K. The PL decay accelerates systematically down the halide series, and each decay curve is fit well to a single exponential function. We hypothesize that this acceleration is primarily due to increased radiative transition probabilities of the emissive d−d excited state associated with that state's increased charge-transfer character, as anticipated from the correspondingly decreasing energies of LMCT transitions down this series. The first LMCT absorption band in CrI_3 has been identified at $E_{CT} \approx 1.9$ eV and in $CrBr_3$ it occurs at $E_{CT} \approx 2.9$ eV,[28] but the one in $CrCl_3$ has not yet been reported. Using Jørgensen's optical electronegativity model[29] and $E_{CT} \approx 2.9$ eV for $CrBr_3$, we estimate that the first LMCT band of $CrCl_3$ will occur at ∼3.6 eV.

Covalency in a metal−ligand complex can be described perturbatively within the molecular-orbital (MO) model in terms of hybridization between the metal's valence orbitals ($|M\rangle$, *e.g.*, 3d or 4f) and symmetry-adapted linear combinations of ligand valence atomic orbitals ($|L_{SALC}>$), as in eq 1.

$$\psi = N(|M> - c|L_{SALC}>) \tag{1}$$

N is a normalization constant. The covalency coefficient (c) is given by eq 2

$$c = \frac{H_{ML}}{\Delta E_{ML}} \approx \frac{H_{ML}}{E_{CT}} \tag{2}$$

where ΔE_{ML} is the energy difference between metal and L_{SALC} orbitals in the absence of mixing, and H_{ML} is the off-diagonal matrix element describing the resonance energy associated with $M-L_{SALC}$ mixing. The covalent admixture of ligand valence orbitals into the metal valence orbitals is given by c^2. H_{ML} is proportional to the $M-L_{SALC}$ orbital overlap integral, S. The energy difference ΔE_{ML} relates to the difference between metal and ligand valence-shell ionization energies and is approximated by the energy of the complex's lowest-energy LMCT transition ($\Delta E_{ML} \approx E_{CT}$).

The radiative rate constant ($k_{rad} = \frac{1}{\tau_{rad}}$) controlling emission from the metal's valence-shell excited state (*e.g.*, d−d, f−f) is proportional to the corresponding excitation's oscillator strength and is given by[30]

$$k_{rad} = \frac{e^2 n \omega^2}{2\pi\varepsilon_0 m_0 c^3} f_M \tag{3}$$

where n is the refractive index of the material, ω is the intra-shell transition's angular frequency, f_M is its oscillator strength, and the other parameters are fundamental constants. The refractive indices are 1.8, 2.6, and 2.0 for $CrCl_3$, $CrBr_3$, and CrI_3, respectively.[31,32]

Because the ${}^4T_{2g} \rightarrow {}^4A_{2g}$ d−d intra-shell transitions of pseudo-octahedral Cr^{3+} are formally electric-dipole forbidden due to parity, their radiative lifetimes are to first order determined by "intensity borrowing" from parity-allowed LMCT excited states. Microscopically, this process involves mixing of d−d and LMCT configurations and is therefore closely related to covalency. In this scenario, the anticipated trend in d−d oscillator strengths is described to first order as in eq 4,[33,34] where f_{CT} is the allowed LMCT transition's oscillator strength and the bracketed term is very similar to the covalency coefficient, c, of eq 2, with H_{MLu} representing only the odd-parity matrix elements (static or dynamic). Because of energetic proximity, intensity borrowing is dominated by contributions from the metal's intra-shell excited state (at energy E_{ES}) rather than its ground state (at energy $E_{GS} = 0$), and hence the energy denominator in eq 4 is reduced by E_{ES}.

$$f_M \approx \frac{E_{ES}}{E_{CT}}\left[\frac{H_{MLu}}{E_{CT} - E_{ES}}\right]^2 f_{CT} \tag{4}$$

Neglecting changes in f_{CT} and H_{MLu} across the CrX_3 series, eqs 3 and 4, predict relative radiative lifetimes of (1.00):(0.32):(0.10) for Cl:Br:I, in reasonable agreement with the experimental lifetime trend of (1.00):(0.46):(0.11) at 4 K. This simple analysis thus shows that the short PL decay time of the ${}^4T_{2g} \rightarrow {}^4A_{2g}$ transition observed in Figure 3c primarily results from the relatively low LMCT energy of CrI_3, which in turn favors high d-orbital covalency.

Figure 3d shows the 4 K decay dynamics of the narrow Yb^{3+} f−f luminescence in each of the doped CrX_3 compounds. Again, the PL decay accelerates systematically going down the halide series, and each curve fits well to a single-exponential function. The inset shows an enlarged view of the CrI_3:Yb^{3+} PL decay curve. The absence of noticeable rise times in these PL decay curves is consistent with the conclusion of rapid energy migration within the CrX_3 lattices. Whereas the Yb^{3+} PL decay times of ∼970 and 500 μs for $CrCl_3$:Yb^{3+} and $CrBr_3$:Yb^{3+} are comparable to those reported for Yb^{3+} in other chloride and bromide lattices,[35,36] the 8.6 μs Yb^{3+} decay time of CrI_3:Yb^{3+} is extraordinarily short. Although some of this reduction may be due to nonradiative contributions even at 4 K, low-energy LMCT transitions in $[YbI_6]^{3-}$ are also expected to relax intra-shell parity forbiddenness and accelerate radiative decay, as discussed for Cr^{3+} above. The Yb^{3+} LMCT transition energies in these compounds are unknown, but the first LMCT excited states of $[YbX_6]^{3-}$ centers in other chloride, bromide, and iodide compounds have been reported at ∼4.46,[29,37,38] ∼3.60,[29,37,39] and ∼2.21 eV,[29,40] respectively, in each case formally generating $Yb^{2+}(4f^{14})X(np^5)[X^-(np^6)]_5$ final-state configurations.[38] The shifts in these transition energies are consistent with the differences in halide optical electronegativities. From these data, the LMCT energy for Yb^{3+} in CrI_3 is placed ∼0.3 eV higher in energy than the first LMCT transitions of CrI_3 itself (Figure 3a). Direct spectroscopic determination of E_{CT} for Yb^{3+} in CrX_3:Yb^{3+} is thus complicated by the low concentration of Yb^{3+} and the overlapping Cr^{3+} LMCT bands in the same spectral region.

Applying the same analysis described above using these LMCT energies, and taking the highest f−f emission energy in each compound at 4 K as E_{ES}, eqs 3 and 4 predict relative Yb^{3+} radiative lifetimes across this CrX_3:Yb^{3+} series to be (1.00):(0.31):(0.06) for Cl:Br:I, compared to the experimental results of (1.00):(0.52):(0.01) from Figure 3d. Again, we find reasonable agreement (Figure S4) between experiment and expectations from the simple perturbation model of eq 4. Importantly, this analysis also indicates that f-orbital Yb^{3+}−X^- covalency (c^2) increases markedly across the CrX_3:Yb^{3+} series in a ratio of roughly 1:2:10 for Cl:Br:I. The short lifetime of Yb^{3+} in CrI_3 is thus consistent with unusually high f-orbital covalency in this lattice. Although 4f covalency in lanthanides is often considered negligible, $[LnCl_6]^{3-}$ compounds typically

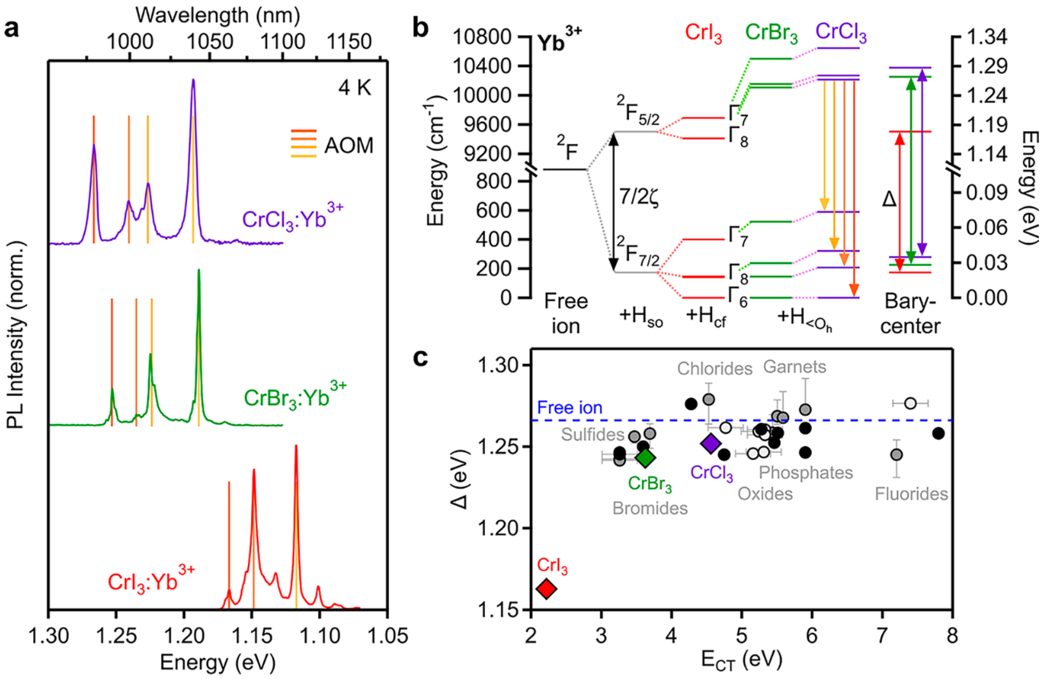

Figure 4. (a) Low-temperature PL data for Yb^{3+}-doped CrX$_3$ (X = Cl, Br, I). The colored vertical sticks indicate the electronic origin assignments used in angular overlap model (AOM) calculations. (b) f-shell spin−orbit and crystal-field splittings for Yb^{3+} ions in CrX$_3$ lattices, from panel (a) and calculated by AOM. The splitting of the ground- and excited-state Γ_8 levels indicates deviation from O_h Yb^{3+} site symmetry. This deviation is more pronounced for the smaller halides. The colored down arrows represent the transitions observed in panel (a). The energy difference between $^2F_{5/2}$ and $^2F_{7/2}$ barycenters is denoted Δ. (c) Plot of the ligand-to-metal charge-transfer (LMCT) energies *vs* Δ for Yb^{3+} ions doped into a variety of lattices. Δ values for CrX$_3$:Yb^{3+} are obtained from panel (a) and AOM calculations, and E_{CT} is taken from literature for other $[YbX_6]^{3-}$ compounds.[29] The black data points represent experimental values for E_{CT} and Δ, the gray data points use experimental values for E_{CT} and semi-experimental values for Δ, and the white data points use experimental values for Δ and values for E_{CT} calculated from Eu^{3+} charge-transfer energies in the same lattice, following the method of Li *et al.*[43] Uncertainties estimated from consideration of multiple literature sources are approximately the size of the CrX$_3$ data points.

have 4f covalencies approaching ∼1%,[41,42] suggesting that f-orbital covalency may reach as high as several percent in CrI$_3$:Yb^{3+}.

Figure 4a shows an enlarged view of the Yb^{3+}-doped CrX$_3$ PL spectra shown in Figure 3b. CrCl$_3$:Yb^{3+} and CrBr$_3$:Yb^{3+} show sharp multi-line spectra at energies that are typical for Cl and Br lattices. Although the spectra are dominated by only a few prominent peaks, careful inspection shows a multitude of nearby lines. We assign the most prominent peaks to electronic origins, as indicated by the colored lines in Figure 4a. The CrI$_3$:Yb^{3+} spectrum occurs at much lower energy than the other two, and its main peaks are more obviously broadened by distinct shoulders. Sideband intensities are also relatively more intense in this spectrum. We again associate the three maxima in this spectrum with electronic origins. Note that the highest-energy maximum in the CrI$_3$:Yb^{3+} PL spectrum has a higher energy shoulder, making precise identification of the true electronic origin uncertain to within ∼2.5 meV.

Figure 4b illustrates the splitting of the Yb^{3+} ^2F free-ion term upon introduction of spin−orbit and crystal-field terms of the molecular Hamiltonian. Using the angular overlap model (AOM)[44] for analysis of these spectra, spin−orbit coupling and crystal-field parameters (Table S2) were adjusted to reproduce the experimental $^2F_{5/2} \rightarrow {}^2F_{7/2}$ transition energies of each compound (colored lines in Figure 4a), from which the energies of the remaining $^2F_{5/2}$ crystal-field levels were extracted. These energies are plotted in Figure 4b for each compound. Barycenters of the $^2F_{5/2}$ and $^2F_{7/2}$ states were then calculated from the crystal-field levels for each compound. The energy difference between $^2F_{5/2}$ and $^2F_{7/2}$ barycenters is denoted by Δ. From Figure 4b, these values of Δ primarily reflect the magnitude of the spin−orbit coupling parameter, Δ ≈ 7/2ζ. For example, the above AOM analysis yields Δ values that differ from 7/2ζ by only 0.81, 0.59, and 0.31 meV (<0.1%) for Yb^{3+} in CrCl$_3$, CrBr$_3$, and CrI$_3$, respectively. Note that although the $^2F_{5/2}$ crystal-field energies in the CrX$_3$:Yb^{3+} compounds are not obtained experimentally, they have relatively little influence on Δ, and essentially indistinguishable results are obtained from simply considering the mean PL energy of each spectrum in Figure 4a.

Inspired by the relationship between covalency and E_{CT} in eq 2, Figure 4c plots Δ *vs* E_{CT} for the three CrX$_3$:Yb^{3+} compounds reported here. This plot also includes additional data points from a wide variety of literature sources for other Yb^{3+}-doped compounds (see Table S3). Select compound classes are labeled in the figure. Previous studies have demonstrated that Δ is generally independent of ligand class,[45,46] consistent with the high shielding and low covalency that typifies the 4f valence shell of trivalent lanthanide ions. This typical behavior is highlighted in Figure 4c, which shows Δ values nearly the same as the free-ion spin−orbit splitting energy for all but one notable exception: CrI$_3$:Yb^{3+}. Δ in this compound is substantially smaller than in any other known Yb^{3+} compound. From its value, ζ is reduced by 9% in CrI$_3$:Yb^{3+} (330 meV) relative to the Yb^{3+} free ion (362 meV). Not coincidentally, CrI$_3$:Yb^{3+} also has the smallest value of E_{CT}, ∼1 eV smaller than for the next closest compounds in Figure 4c. Per eq 2, the data in Figure 4c thus support the conclusion that the anomalously small value of Δ in $CrI_3:Yb^{3+}$ is attributable to exceptionally high f-orbital covalency in this compound, which in turn arises from the shallow valence-shell ionization energy of the iodide ligands relative to other ligands in this figure. This interpretation supports the conclusion drawn from analysis of the PL decay times in Figure 3d.

In addition to the low LMCT energies (E_{CT} in eq 2), the large size discrepancy between Yb^{3+} and Cr^{3+} ($r_{Yb}/r_{Cr} = 1.41$) may also contribute to high covalency by effectively forcing the X^- ligands toward the Yb^{3+} dopant, thereby increasing orbital overlap (and hence increasing H_{ML} in eq 2). To assess the importance of this kind of "internal pressure", it is interesting to compare Δ in $CrBr_3:Yb^{3+}$ with that found in $NaYS_2:Yb^{3+}$.[47] Both lattices have octahedral coordination of Yb^{3+} and show similar values of E_{CT} (∼3.26 eV). The ionic radii of Br^- (196 pm) and S^{2-} (184 pm) are also similar, but in the latter Yb^{3+} substitutes for Y^{3+}, which has a substantially larger ionic radius than Cr^{3+} (90 *vs* 62 pm). Nevertheless, Δ in $NaYS_2:Yb^{3+}$ is very similar to that in $CrBr_3:Yb^{3+}$ (Figure 4c, Table S3). This comparison suggests that E_{CT} is the dominant factor differentiating covalency in these compounds, not H_{ML}.

An additional consideration is the effect of anion spin−orbit coupling on Δ. The spin−orbit coupling constant of iodine, 581 meV (4690 cm^{-1}),[48] greatly exceeds even that of Yb^{3+} [362 meV (2918 cm^{-1}) in the Yb^{3+} free ion]. Anion SOC is thus no longer negligible in $CrI_3:Yb^{3+}$, in contrast with most of the compounds in Figure 4c, and given the relatively high covalency in $CrI_3:Yb^{3+}$ this factor may influence the spectroscopic splitting, Δ. For example, sulfides have much smaller ligand SOC constants [36 meV (288 cm^{-1})]. We note that a few examples of Yb^{3+}-doped tellurides have been reported,[49] which should have similar values for both E_{CT} and ligand SOC compared to $CrI_3:Yb^{3+}$. Direct comparison with $CrI_3:Yb^{3+}$ is precluded by the fact that these tellurides all have tetrahedral coordination of Yb^{3+}, however. This low coordination number is expected to reduce the total f-orbital covalency, and indeed their Δ values are again similar to the free ion. Further investigation will be required to elucidate the impact of two-center SOC in such compounds.

Overall, these data contribute to the more general discussion of f-orbital covalency in lanthanides and actinides that has recently drawn broad attention, primarily in molecular contexts.[41,50−53] The present data provide strong evidence for so-called "degeneracy-driven" covalency in the $[YbX_6]^{3-}$ units of $CrX_3:Yb^{3+}$ compounds across the Cl → Br → I composition series, based on systematic trends correlated with anion electronegativity and comparison to other lattices. Indeed, the entire Yb^{3+} data set in Figure 4c appears to follow a trend of the form $\Delta = 7/2\zeta_{\text{free ion}} - (\text{const.}/E_{CT})^2$, albeit with some scatter. We also note that the Yb^{3+} barycenter trend in Figure 4 upon going from Cl → I is far more pronounced than those typically observed for other lanthanide compounds of the same halides. For example, whereas $\Delta(I)/\Delta(Cl) \sim 92.8\%$ in $CrX_3:Yb^{3+}$, the average ratio of visible and near-IR Δ values in $Cs_3Er_2X_9$ compounds[54] is $\Delta_{avg}(I)/\Delta_{avg}(Cl) \sim 99.9\%$. For the Er^{3+} multiplet closest in energy to the Yb^{3+} $^2F_{5/2}$ state ($^4I_{11/2}$), this ratio is $\Delta(I)/\Delta(Cl) \sim 100.0\%$. Yb^{3+} is the second most easily reduced trivalent lanthanide behind only Eu^{3+}, and hence it has comparatively low charge-transfer energies. Er^{3+} CT states are expected ∼1.8 eV higher in energy than those of Yb^{3+} with the same coordination,[37,55] which translates to a reduction in ground-state covalency c^2 by a factor of ∼3.3 in $[ErI_6]^{3-}$ relative to $[YbI_6]^{3-}$. This comparison thus supports the conclusion that ΔE_{ML} (or E_{CT}, eq 2) dominates over H_{ML} in enhancing the f-orbital covalency of Yb^{3+} in CrI_3.

Finally, and remarkably, we note that Yb^{3+} f−f PL has apparently not been reported for Yb^{3+} in any other iodide lattice. In fact, surprisingly few compounds involving $[YbI_6]^{3-}$ octahedra have been reported at all,[25,40,56,57] and no f−f spectra have been reported for those compounds. Thus, at this moment, no conclusions can be drawn about whether $CrI_3:Yb^{3+}$ typifies iodides or is in some way also distinct within this class. The scarcity of $[YbI_6]^{3-}$ f−f data is likely related to the same relative ease of Yb^{3+} reduction that leads to its enhanced covalency; $[EuI_6]^{3-}$ compounds appear to be even more rare, but both Yb^{2+} and Eu^{2+} iodides are well known.[58−60] Experiments are under way to develop other Yb^{3+}-doped iodides for deeper exploration of this rare motif, from which our preliminary results show that other iodides also fall well below the distribution represented by the other compounds in Figure 4c; these findings support the above analyses and will be reported separately.

CONCLUSIONS

In conclusion, we have demonstrated successful incorporation of Yb^{3+} dopants into $CrCl_3$, $CrBr_3$, and CrI_3 van der Waals lattices. EXAFS data show Yb−X bond lengths that are ∼0.25 Å larger than their Cr−X counterparts, and data fitting shows structures consistent with Yb^{3+} substituting for Cr^{3+} (or occupying the comparable antisite) despite its ∼1.4× larger ionic radius. PL measurements demonstrate efficient energy transfer from Cr^{3+} to Yb^{3+}, resulting in complete quenching of the broad Cr^{3+} d−d luminescence and appearance of sharp Yb^{3+} f−f luminescence at modest Yb^{3+} doping levels. TRPL measurements show an exceptionally short excited-state lifetime of only 8.6 μs for Yb^{3+} in $CrI_3:Yb^{3+}$ at 4 K. Energetically, the $CrI_3:Yb^{3+}$ PL spectrum is also significantly redshifted compared to those of $CrBr_3:Yb^{3+}$ and $CrCl_3:Yb^{3+}$. Data analysis and AOM calculations show that this shift is due to an anomalously small $^2F_{7/2}$-$^2F_{5/2}$ spin−orbit splitting in $CrI_3:Yb^{3+}$. Broader comparison to Yb^{3+} in a wide variety of other lattices shows that the low PL energy of $CrI_3:Yb^{3+}$ is in fact an outlier across *all* investigated materials. We propose that the low energy and short decay time of $CrI_3:Yb^{3+}$ PL are both attributable to anomalously high Yb−I f-orbital covalency, ultimately stemming from the shallow valence-shell ionization potentials of the iodide ligands. Beyond demonstrating Yb^{3+} doping as an effective approach to narrowing the emission of the entire family of CrX_3 2D van der Waals ferromagnets, these results provide rare fundamental insights into the electronic structure and luminescence of the remarkably underexplored $[YbI_6]^{3-}$ motif, revealing it to be an outlier among known Yb^{3+} compounds because of its exceptionally high f-orbital covalency. In addition to the above manifestations, this high covalency has important physical consequences for the promotion of strong Yb^{3+}−Cr^{3+} magnetic superexchange in $CrI_3:Yb^{3+}$.[15]

ASSOCIATED CONTENT

Supporting Information

The Supporting Information is available free of charge at https://pubs.acs.org/doi/10.1021/jacs.3c05989.

Additional experimental details, including sample preparation and characterization, additional EXAFS data and fitting, as well as fit parameters, additional structural characterization in the form of SEM and EDX images, parameters as used in AOM calculations, and a full table pertaining to the data points used in Figure 4c (PDF)

AUTHOR INFORMATION

Corresponding Author

Daniel R. Gamelin − *Department of Chemistry, University of Washington, Seattle, Washington 98195, United States;* orcid.org/0000-0003-2888-9916; Email: gamelin@uw.edu

Authors

Thom J. Snoeren − *Department of Chemistry, University of Washington, Seattle, Washington 98195, United States;* orcid.org/0000-0001-8055-3710

Kimo Pressler − *Department of Chemistry, University of Washington, Seattle, Washington 98195, United States;* orcid.org/0000-0003-2788-1592

Kyle T. Kluherz − *Department of Chemistry, University of Washington, Seattle, Washington 98195, United States; Physical Sciences Division, Pacific Northwest National Laboratory, Richland, Washington 99352, United States;* orcid.org/0000-0002-7986-5167

Kelly M. Walsh − *Department of Chemistry, University of Washington, Seattle, Washington 98195, United States;* orcid.org/0000-0001-5349-8816

James J. De Yoreo − *Physical Sciences Division, Pacific Northwest National Laboratory, Richland, Washington 99352, United States;* orcid.org/0000-0002-9194-6699

Complete contact information is available at: https://pubs.acs.org/10.1021/jacs.3c05989

Notes

The authors declare no competing financial interest.

ACKNOWLEDGMENTS

Support of this project by the US NSF (DMR-1807394) is gratefully acknowledged. Additional support was received from the UW Clean Energy Institute (graduate fellowships to T.J.S. and K.M.W.). Part of this work was conducted at the Molecular Analysis Facility, a National Nanotechnology Coordinated Infrastructure (NNCI) site at the University of Washington that is supported in part by the National Science Foundation (NNCI-1542101 and NNCI-2025489), the University of Washington, the Molecular Engineering & Sciences Institute, the Clean Energy Institute, and the National Institutes of Health. EXAFS measurements were supported by the UW Molecular Engineering Materials Center, an NSF Materials Research Science and Engineering Center (grant no. DMR-1719797). This research used resources of the Advanced Photon Source, a U.S. Department of Energy (DOE) Office of Science User Facility operated for the DOE Office of Science by Argonne National Laboratory under Contract no. DE-AC02-06CH11357. We acknowledge S. Heald and S. Kelly from APS Sector 20 (BL 20-BM) (GUP 77348) for collecting these data sets and assistance with data processing. We also thank S. Mergelsberg and S. Saslow for their assistance with EXAFS theory and analysis.

REFERENCES

(1) Huang, B.; Clark, G.; Navarro-Moratalla, E.; Klein, D. R.; Cheng, R.; Seyler, K. L.; Zhong, D.; Schmidgall, E.; McGuire, M. A.; Cobden, D. H.; Yao, W.; Xiao, D.; Jarillo-Herrero, P.; Xu, X. Layer-Dependent Ferromagnetism in a van der Waals Crystal Down to the Monolayer Limit. *Nature* **2017**, *546*, 270−273.

(2) Burch, K. S.; Mandrus, D.; Park, J.-G. Magnetism in Two-Dimensional van der Waals Materials. *Nature* **2018**, *563*, 47−52.

(3) Duong, D. L.; Yun, S. J.; Lee, Y. H. Van der Waals Layered Materials: Opportunities and Challenges. *ACS Nano* **2017**, *11*, 11803−11830.

(4) Liu, Y.; Huang, Y.; Duan, X. Van der Waals Integration Before and Beyond Two-Dimensional Materials. *Nature* **2019**, *567*, 323−333.

(5) Dillon, J. F.; Olson, C. E. Magnetization, Resonance, and Optical Properties of the Ferromagnet CrI_3. *J. Appl. Phys.* **1965**, *36*, 1259−1260.

(6) Seyler, K. L.; Zhong, D.; Klein, D. R.; Gao, S.; Zhang, X.; Huang, B.; Navarro-Moratalla, E.; Yang, L.; Cobden, D. H.; McGuire, M. A.; Yao, W.; Xiao, D.; Jarillo-Herrero, P.; Xu, X. Ligand-Field Helical Luminescence in a 2D Ferromagnetic Insulator. *Nat. Phys.* **2018**, *14*, 277−281.

(7) Güdel, H. U.; Snellgrove, T. R. Jahn-Teller Effect in the $^4T_{2g}$ State of Chromium(III) in Dicesium Sodium Indium(III) Hexachloride. *Inorg. Chem.* **1978**, *17*, 1617−1620.

(8) Dillon, J. F.; Kamimura, H.; Remeika, J. P. Magnetic Rotation of Visible Light by Ferromagnetic $CrBr_3$. *Phys. Rev. Lett.* **1962**, *9*, 161−163.

(9) Dillon, J. F.; Kamimura, H.; Remeika, J. P. Magneto-Optical Properties of Ferromagnetic Chromium Trihalides. *J. Phys. Chem. Solids* **1966**, *27*, 1531−1549.

(10) Limido, C.; Pedroli, G.; Spinolo, G. Specific Magnetic Rotation in the Crystal Field Bands of $CrCl_3$. *Solid State Commun.* **1972**, *11*, 1385−1388.

(11) Nosenzo, L.; Samoggia, G.; Pollini, I. Effect of Magnetic Ordering on the Optical Properties of Transition-Metal Halides: $NiCl_2$, $NiBr_2$, $CrCl_3$, and $CrBr_3$. *Phys. Rev. B* **1984**, *29*, 3607−3616.

(12) Borghesi, A.; Guizzetti, G.; Samoggia, G.; Reguzzoni, E. Magneto-Optical Effects in the Paramagnetic and Ferromagnetic Phases of $CrBr_3$. *Phys. Rev. Lett.* **1981**, *47*, 538−541.

(13) Zhang, Z.; Shang, J.; Jiang, C.; Rasmita, A.; Gao, W.; Yu, T. Direct Photoluminescence Probing of Ferromagnetism in Monolayer Two-Dimensional $CrBr_3$. *Nano Lett.* **2019**, *19*, 3138−3142.

(14) Cai, X.; Song, T.; Wilson, N. P.; Clark, G.; He, M.; Zhang, X.; Taniguchi, T.; Watanabe, K.; Yao, W.; Xiao, D.; McGuire, M. A.; Cobden, D. H.; Xu, X. Atomically Thin $CrCl_3$: An In-Plane Layered Antiferromagnetic Insulator. *Nano Lett.* **2019**, *19*, 3993−3998.

(15) Pressler, K.; Snoeren, T. J.; Walsh, K. M.; Gamelin, D. R. Magnetic Amplification at Yb^{3+} "Designer Defects" in the van der Waals Ferromagnet CrI_3. *Nano Lett.* **2023**, *23*, 1320−1326.

(16) Morosin, B.; Narath, A. X-Ray Diffraction and Nuclear Quadrupole Resonance Studies of Chromium Trichloride. *J. Chem. Phys.* **1964**, *40*, 1958−1967.

(17) Kozlenko, D. P.; Lis, O. N.; Kichanov, S. E.; Lukin, E. V.; Belozerova, N. M.; Savenko, B. N. Spin-Induced Negative Thermal Expansion and Spin−Phonon Coupling in van der Waals Material $CrBr_3$. *npj Quantum Mater.* **2021**, *6*, 19.

(18) McGuire, M. A.; Dixit, H.; Cooper, V. R.; Sales, B. C. Coupling of Crystal Structure and Magnetism in the Layered, Ferromagnetic Insulator CrI_3. *Chem. Mater.* **2015**, *27*, 612−620.

(19) Shannon, R. Revised Effective Ionic Radii and Systematic Studies of Interatomic Distances in Halides and Chalcogenides. *Acta Crystallogr. A* **1976**, *32*, 751−767.

(20) Ravel, B.; Newville, M. ATHENA, ARTEMIS, HEPHAESTUS: Data Analysis for X-Ray Absorption Spectroscopy Using IFEFFIT. *J. Synchrotron Radiat.* **2005**, *12*, 537−541.

(21) Pizzochero, M. Atomic-Scale Defects in the Two-Dimensional Ferromagnet CrI_3 from First Principles. *J. Phys. D: Appl. Phys.* **2020**, *53*, 244003.

(22) Braekken, H. The Crystal Structure of Chromium Tribromide (Eng. Transl.). *K. Nor. Vidensk. Selsk.* **1932**, *5*, 42.

(23) Templeton, D. H.; Carter, G. F. The Crystal Structures of Yttrium Trichloride and Similar Compounds. *J. Phys. Chem.* **1954**, *58*, 940−944.

(24) Brenner, M. *Kinetic Studies of Phase Transformations between Polymorphic Forms of Ytterbium(II) Bromide and Determination of the Crystal Structure of Ytterbium(III) Bromide Considering the Stacking Disorder of the Crystals Used (Eng. Transl.)*; Universität Karlsruhe, 1997.

(25) Asprey, L. B.; Keenan, T. K.; Kruse, F. H. Preparation and Crystal Data for Lanthanide and Actinide Triiodides. *Inorg. Chem.* **1964**, *3*, 1137−1141.

(26) Emge, T. J.; Kornienko, A.; Brennan, J. G. Trans Influence in a Mer-Octahedral Triiodidolanthanide: Triiodidotris(Tetrahydrofuran-κO)Ytterbium(III). *Acta Crystallogr. C* **2009**, *65*, m422−m425.

(27) Zhang, J.; Guo, Y.; Li, P.; Wang, J.; Zhou, S.; Zhao, J.; Guo, D.; Zhong, D. Imaging Vacancy Defects in Single-Layer Chromium Triiodide. *J. Phys. Chem. Lett.* **2021**, *12*, 2199−2205.

(28) De Siena, M. C.; Creutz, S. E.; Regan, A.; Malinowski, P.; Jiang, Q.; Kluherz, K. T.; Zhu, G.; Lin, Z.; De Yoreo, J. J.; Xu, X.; Chu, J.-H.; Gamelin, D. R. Two-Dimensional van der Waals Nanoplatelets with Robust Ferromagnetism. *Nano Lett.* **2020**, *20*, 2100−2106.

(29) Jørgensen, C. K. Electron Transfer Spectra. *Progress in Inorganic Chemistry*; John Wiley & Sons, Inc., 1970; Vol. *12*, pp 101−158.

(30) ’t Hooft, G. W.; Van der Poel, W. A. J. A.; Molenkamp, L. W.; Foxon, C. T. Giant Oscillator Strength of Free Excitons in GaAs. *Phys. Rev. B* **1987**, *35*, 8281−8284.

(31) Bermudez, V. M.; McClure, D. S. Spectroscopic Studies of the Two-Dimensional Magnetic Insulators Chromium Trichloride and Chromium Tribromide—I. *J. Phys. Chem. Solids* **1979**, *40*, 129−147.

(32) Tomarchio, L.; Macis, S.; Mosesso, L.; Nguyen, L. T.; Grilli, A.; Guidi, M. C.; Cava, R. J.; Lupi, S. Low Energy Electrodynamics of CrI_3 Layered Ferromagnet. *Sci. Rep.* **2021**, *11*, 23405.

(33) Ballhausen, C. J. *Introduction to Ligand Field Theory*; McGraw-Hill: New York, 1962; pp 185−188.

(34) Solomon, E. I. Inorganic Spectroscopy: An Overview. *Comments Inorg. Chem.* **1984**, *3*, 225−320.

(35) Mir, W. J.; Mahor, Y.; Lohar, A.; Jagadeeswararao, M.; Das, S.; Mahamuni, S.; Nag, A. Postsynthesis Doping of Mn and Yb into $CsPbX_3$ (X = Cl, Br, or I) Perovskite Nanocrystals for Downconversion Emission. *Chem. Mater.* **2018**, *30*, 8170−8178.

(36) Chen, N.; Cai, T.; Li, W.; Hills-Kimball, K.; Yang, H.; Que, M.; Nagaoka, Y.; Liu, Z.; Yang, D.; Dong, A.; Xu, C.-Y.; Zia, R.; Chen, O. Yb- and Mn-Doped Lead-Free Double Perovskite Cs_2AgBiX_6 (X = Cl^-, Br^-) Nanocrystals. *ACS Appl. Mater. Interfaces* **2019**, *11*, 16855−16863.

(37) Dorenbos, P.; Josef, A.; De Haas, J. T. M.; Krämer, K. W. Vacuum Referred Binding Energies of the Lanthanides in Chloride, Bromide, and Iodide Compounds. *J. Lumin.* **2019**, *208*, 463−467.

(38) Ryan, J. L.; Jørgensen, C. K. Absorption Spectra of Octahedral Lanthanide Hexahalides. *J. Phys. Chem.* **1966**, *70*, 2845−2857.

(39) Gafurov, M. R.; Iskhakova, A. I.; Kurkin, I. N.; Kurzin, S. P.; Boris, Z. M.; Sergey, I. N.; Orlinskii, S. B.; Rakhmatullin, R. M.; Gil’man, S. S.; Valery, F. T.; Demirbilek, R.; Heber, J. Spectra and Relaxation of Electronic Excitations in $CsCdBr_3$:Yb^{3+} and $CsCdBr_3$:Nd^{3+} Monocrystals. *Proc. SPIE 4766, XI Feofilov Symposium on Spectroscopy of Crystals Activated by Rare-Earth and Transition Metal Ions*; SPIE, 2002; Vol. *4766*, pp 279−291.

(40) Ryan, J. L. Weak or Unstable Iodo Complexes. I. Hexaiodo Complexes of the Lanthanides. *Inorg. Chem.* **1969**, *8*, 2053−2058.

(41) Löble, M. W.; Keith, J. M.; Altman, A. B.; Stieber, S. C. E.; Batista, E. R.; Boland, K. S.; Conradson, S. D.; Clark, D. L.; Lezama Pacheco, J.; Kozimor, S. A.; Martin, R. L.; Minasian, S. G.; Olson, A. C.; Scott, B. L.; Shuh, D. K.; Tyliszczak, T.; Wilkerson, M. P.; Zehnder, R. A. Covalency in Lanthanides. An X-ray Absorption Spectroscopy and Density Functional Theory Study of $LnCl_6^{x-}$ (x = 3, 2). *J. Am. Chem. Soc.* **2015**, *137*, 2506−2523.

(42) Atanasov, M.; Daul, C.; Güdel, H. U.; Wesolowski, T. A.; Zbiri, M. Ground States, Excited States, and Metal−Ligand Bonding in Rare Earth Hexachloro Complexes: A DFT-Based Ligand Field Study. *Inorg. Chem.* **2005**, *44*, 2954−2963.

(43) Li, L.; Zhou, S.; Zhang, S. Relationship Between Charge Transfer Energies of Yb^{3+} and Sm^{3+} and Crystal Environmental Factor. *J. Lumin.* **2009**, *129*, 187−191.

(44) Bronova, A.; Bredow, T.; Glaum, R.; Riley, M. J.; Urland, W. BonnMag: Computer Program for Ligand-Field Analysis of f^n Systems Within the Angular Overlap Model. *J. Comput. Chem.* **2018**, *39*, 176−186.

(45) Antic-Fidancev, E. Simple Way to Test the Validity of $^{2S+1}L_J$ Barycenters of Rare Earth Ions (e.g. $4f^2$, $4f^3$ and $4f^6$ Configurations). *J. Alloys Compd.* **2000**, *300−301*, 2−10.

(46) Haumesser, P.-H.; Gaumé, R.; Viana, B.; Antic-Fidancev, E.; Vivien, D. Spectroscopic and Crystal-Field Analysis of New Yb-Doped Laser Materials. *J. Phys. Condens. Matter* **2001**, *13*, 5427−5447.

(47) Hansen, P.-A.; Kumar, S.; Meijerink, A. Strong Self-Sensitized Green and NIR Emission in $NaYS_2$ Doped with Pr^{3+} and Yb^{3+} by Inducing Laporte Allowed and Charge Transfer Transitions. *J. Lumin.* **2021**, *235*, 118012.

(48) Martin, W. C. Table of Spin-Orbit Energies for p-Electrons in Neutral Atomic (core)np Configurations. *J. Res. Natl. Inst. Stand. Technol.* **1971**, *75A*, 109−111.

(49) Bryant, F. J. Ion Implanation in Group II−VI Compounds. *Prog. Cryst. Growth Char.* **1983**, *6*, 191−263.

(50) Neidig, M. L.; Clark, D. L.; Martin, R. L. Covalency in f-Element Complexes. *Coord. Chem. Rev.* **2013**, *257*, 394−406.

(51) Kerridge, A. Quantification of f-Element Covalency Through Analysis of the Electron Density: Insights from Simulation. *Chem. Commun.* **2017**, *53*, 6685−6695.

(52) Vitova, T.; Pidchenko, I.; Fellhauer, D.; Bagus, P. S.; Joly, Y.; Pruessmann, T.; Bahl, S.; Gonzalez-Robles, E.; Rothe, J.; Altmaier, M.; Denecke, M. A.; Geckeis, H. The Role of the 5f Valence Orbitals of Early Actinides in Chemical Bonding. *Nat. Commun.* **2017**, *8*, 16053.

(53) Vitova, T.; Roesky, P. W.; Dehnen, S. Open Questions on Bonding Involving Lanthanide Atoms. *Commun. Chem.* **2022**, *5*, 12.

(54) Hehlen, M. P.; Krämer, K.; Güdel, H. U.; McFarlane, R. A.; Schwartz, R. N. Upconversion in Er^{3+}-Dimer Systems: Trends Within the Series $Cs_3Er_2X_9$ (X=Cl,Br,I). *Phys. Rev. B* **1994**, *49*, 12475−12484.

(55) Dorenbos, P. Systematic Behaviour in Trivalent Lanthanide Charge Transfer Energies. *J. Phys. Condens. Matter* **2003**, *15*, 8417−8434.

(56) Arumugam, G. M.; Xu, C.; Karunakaran, S. K.; Shi, Z.; Zhu, C.; Wei, M.; Feifei, Q. Efficient Red Up-Conversion Emission from Er^{3+}-Yb^{3+} Co-Doped Rubidium Lead Iodide Perovskite Nanowires with Surface Plasmons. *Appl. Phys. Lett.* **2018**, *112*, 054104.

(57) Shi, J.; Li, F.; Yuan, J.; Ling, X.; Zhou, S.; Qian, Y.; Ma, W. Efficient and Stable $CsPbI_3$ Perovskite Quantum Dots Enabled by In Situ Ytterbium Doping for Photovoltaic Applications. *J. Mater. Chem. A* **2019**, *7*, 20936−20944.

(58) Meyer, G. The Divalent State in Solid Rare Earth Metal Halides. *The Rare Earth Elements: Fundamentals and Applications*; Wiley, 2012, p 161.

(59) Rubio, O. J. Doubly-Valent Rare-Earth Ions in Halide Crystals. *J. Phys. Chem. Solids* **1991**, *52*, 101−174.

(60) Dorenbos, P. Energy of the First $4f^7$→$4f^65d$ Transition of Eu^{2+} in Inorganic Compounds. *J. Lumin.* **2003**, *104*, 239−260.

https://doi.org/10.1021/jacs.3c05989
J. Am. Chem. Soc. 2023, 145, 17427−17434